ACS APPLIED ELECTRONIC MATERIALS

pubs.acs.org/acsaelm

Article

High-Temperature Ultrasensitive FET-Based CVD Graphene Hall Probes

Linda Supalová, Miroslav Bartošík,* Vojtěch Švarc, Jindřich Mach, Jakub Piastek, Ondřej Špaček, Martin Konečný, and Tomáš Šikola

Cite This: ACS Appl. Electron. Mater. 2025, 7, 5889−5897

Read Online

ACCESS | Metrics & More | Article Recommendations | Supporting Information

ABSTRACT: Hall probes play a critical role in industrial applications such as electrical compasses, current sensors, and motion detectors; however, their performance often deteriorates at high temperatures. This study presents a magnetic-field probe with an ultrahigh sensitivity of 880 Ω/T at 150 °C, achieved using a graphene Hall bar integrated into a field-effect transistor (FET) architecture. To attain this exceptional sensitivity at elevated temperatures, careful control of doping, passivation, and manufacturing defects is essential. The doping level is optimized by adjusting the gate voltage to maintain the carrier concentration near the charge neutrality point (CNP). Further improvements in sensor response at high temperatures, as well as nearly a 2-fold increase in sensitivity at room temperature, are realized through polymer passivation of graphene. In contrast, it is demonstrated that patterning graphene into a narrower channel can increase the number of defects, which reduces the Hall probe's sensitivity. These findings demonstrate the potential of CVD graphene as a durable and high-performance material for Hall probes in challenging environments.

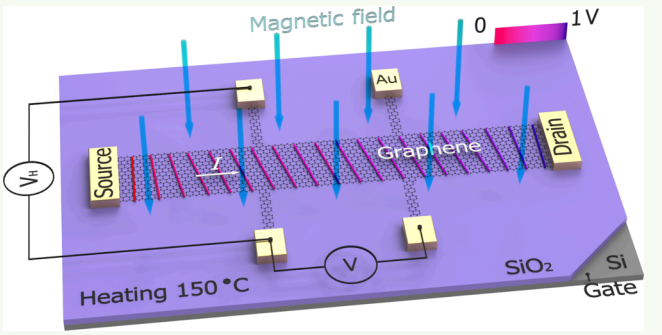

KEYWORDS: *graphene, Hall probe, field-effect transistor, sensitivity, high temperature*

1. INTRODUCTION

Hall probes represent a versatile type of sensor widely used in manufacturing, automotive, and communication systems.[1−4] Their operational principle is based on the well-known Hall effect, in which an applied magnetic field induces a potential difference across an active element with current flowing through the material. The Hall effect does not impose restrictions on the temperature or magnitude of the magnetic field, in contrast to sensors based on the giant magnetoresistance effect (GMR), which struggle at high temperatures due to the limited thermal stability of the multilayer thin films.[5] As such, the Hall probes are also suited for applications requiring an operation at high temperatures and/or strong magnetic fields, for example, for monitoring of conditions inside nuclear fusion research reactors,[6] speed sensing of engine rotors, safety position sensors in steel and metal tempering plants, or current sensing in electronic circuits with limited cooling options.

In order to maximize sensitivity, most Hall probes utilize thin layers of semiconductors with a low charge carrier density (e.g., Si,[7] InAs/GaSb,[8] InSb[9]) as the sensing material. Following this approach, graphene is an ideal candidate for Hall effect sensors due to its atomical thickness and low carrier density near the charge neutrality point combined with relatively high carrier mobility and low electronic noise. Furthermore, the electronic properties of graphene can be tuned by electrostatic gating in a field effect transistor configuration to optimize the sensor performance. Graphene Hall probes have already been studied extensively from low to room temperature, with and without gating effects,[10−15] and these sensors were shown to exhibit a current-related sensitivity defined by the Hall coefficient as high as 6840 Ω/T at room temperature for ultraclean exfoliated graphene encapsulated in hBN.[12] Dai et al. demonstrated the possibility of integrating a graphene Hall probe with CMOS processing circuits in order to increase the sensitivity over 60×.[16] Nonetheless, few studies have tested graphene Hall probes at elevated temperatures, so far with inconsistent results.

Hall probes fabricated from epitaxial graphene were thermally stable from room temperature up to 300 °C with sensitivities of 80 Ω/T[17] and 100 Ω/T,[6] respectively. Similarly, Hall probes based on chemical vapor deposition (CVD) graphene exhibited a stable sensitivity of 40 Ω/T from room

Received: February 19, 2025
Revised: June 5, 2025
Accepted: June 6, 2025
Published: June 18, 2025

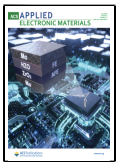

https://doi.org/10.1021/acsaelm.5c00351
ACS Appl. Electron. Mater. 2025, 7, 5889−5897

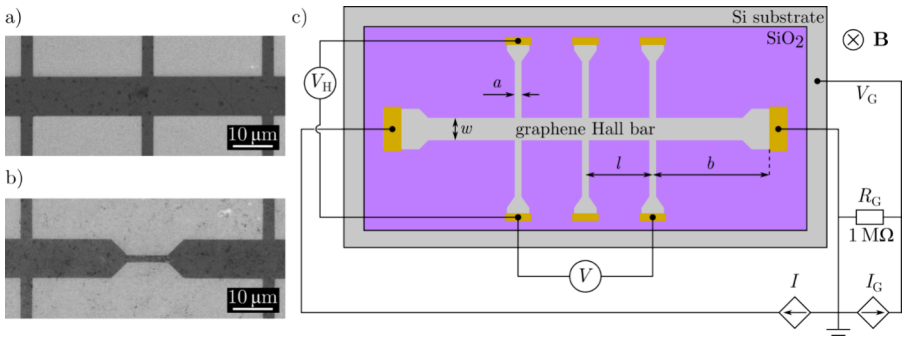

Figure 1. Images of the fabricated graphene Hall bar and a schematic of the electronic measurement setup. SEM image of an 8-contact Hall bar (a) and a constricted 6-contact Hall bar (b). The electronic setup (c) enables simultaneous measurement of the Hall effect and transport properties of the graphene Hall bar.

temperature to 200 °C.[18] Nevertheless, given the low sensitivity values and the lack of any gating mechanism, it is highly probable that these studies were operating in a high charge carrier density regime of graphene, which often shows different behavior compared to the low charge carrier density regime near the charge neutrality point. He et al.[19] used molecular doping on epitaxial graphene Hall probes and found that only heavily doped devices were thermally stable, whereas devices doped closer to the charge neutrality point showed a linear decrease in sensitivity from room temperature to 120 °C.[19] However, molecular doping is an imprecise technique with insufficient control over the results. Consequently, the study was limited only to a few selected charge carrier densities and the molecules were desorbing from graphene at increasing temperature.

This work presents a systematic study of the performance of graphene Hall probes in the temperature interval ranging from room temperature up to 150 °C. The devices have been designed as field effect transistors (FETs) with a solid-state bottom gate for electrostatic doping, and the graphene Hall bar structures enable simultaneous measurement of the Hall effect and transport properties of graphene. In addition to doping, the effect of a passivation layer applied on top of graphene and the influence of defects in the graphene channel induced by channel constriction have also been studied. By combining the passivation layer with the FET-based design, we have achieved the highest reported sensitivity values for graphene Hall probes at 150 °C. Finally, the presented results offer a comprehensive insight into the operation of graphene Hall probes at elevated temperatures, as well as their prospects and limits in potential applications.

2. METHODOLOGY

2.1. Sample Preparation. Graphene Hall probes were fabricated using standard micro/nanofabrication techniques. First, n-doped silicon (100) substrates with a 285 nm layer of dry thermal SiO_2 were patterned with metal contacts in two lithographic steps combining UV lithography and electron beam evaporation. The two-step design reflects considerations for the subsequent transfer of graphene grown by chemical vapor deposition (CVD) and the need for electrical connections to measure transport properties. In the first step, thin Ti(5 nm)/Au(25 nm) electrodes were fabricated around the intended Hall bar positions to minimize the possible tearing of the graphene layer in these areas. In the second fabrication step, thick Ti(5 nm)/Au(100 nm) electrodes and bonding pads were connected to the thin electrodes. Next, CVD graphene grown on a copper foil (purchased from Graphenea) was transferred onto the prepatterned substrates using a standard PMMA-assisted wet transfer method.[20] Afterward, the graphene layer was patterned by electron beam lithography (EBL) and reactive ion etching (RIE) in oxygen plasma into graphene Hall bars contacted by the thin Ti/Au electrodes. Additionally, selected samples were covered by a 500 nm protective layer of SU-8 photoresist to protect the graphene Hall bar from air adsorbents and to stabilize the behavior of the Hall probe during the experiment by suppressing hysteresis caused by adsorbed water. Finally, the prepared chips were glued with conductive silver paint and wire-bonded onto printed circuit boards.

The main dimensions of the graphene Hall bar are the width of the main channel (w = 10 μm), width of the side channels (a = 3 μm), distance between the side channels (l = 30−60 μm), and distance between the side channel and the gold current electrode (b = 60 μm), where the dimension ratios comply with the rules of the American Society for Testing and Materials standard.[21] Furthermore, some Hall bars are constricted in the middle of the main channel to 1 μm width to enhance the influence of edges and defects in these devices. Scanning electron microscope (SEM) images of a standard 8-contact Hall bar and a constricted 6-contact Hall bar are shown in Figure 1a,b. The quality of the fabricated graphene Hall bars was also assessed by Raman spectroscopy measurements (Supporting Information, Figure S1).

2.2. Experiment. Transport properties of graphene and the Hall effect were measured simultaneously under ambient conditions (25 °C, 35% relative humidity) by a four-probe method on the prepared graphene Hall bars with an option to heat the samples from room temperature up to 150 °C. The sample was placed in a holder between a pair of large ferrite magnets with an area of 5 × 5 cm^2 to ensure a uniform external magnetic field across the whole sample. The assumption of the field uniformity was supported by COMSOL Multiphysics simulations (Supporting Information, Figure S6). Furthermore, the distance between the magnets could be adjusted to alter the magnitude of the magnetic field. To facilitate heating during experiments, the sample was placed onto a thin aluminum holder with a heating element (a planar series resistor) on the backside. The temperature was then measured by a Pt100 sensor inserted and affixed by a thermal paste inside the aluminum holder. The assumption was made that the temperature distribution was relatively uniform across the individual parts (the silicon chip, aluminum chip expander, and aluminum holder). Consequently, the temperature sensed by

https://doi.org/10.1021/acsaelm.5c00351
ACS Appl. Electron. Mater. 2025, 7, 5889−5897

the Pt100 sensor has been considered a representative value for the graphene Hall probe.

In the electronic measurement (as shown schematically in Figure 1c), a constant current $I = (1-10)\ \mu A$ was supplied to the main channel of the graphene Hall bar by a Keithley AC and DC Current Source 6221. The longitudinal voltage V and the transverse Hall voltage V_H were measured by a pair of Keithley 2182A Nanovoltmeters on the side channels of the graphene Hall bar. Another Keithley AC and DC Current Source 6221 was used to apply the gate voltage V_G between the silicon substrate and the graphene layer by flowing gate current I_G through a gate resistor R_G. During each transport and Hall effect measurement, the magnetic field and temperature were held constant, only the gate voltage V_G was swept from 0 to 80 V and back to 0 V.

3. RESULTS AND DISCUSSION

3.1. Results. The results of the simultaneous measurement of the longitudinal voltage V and the transverse Hall voltage V_H in dependence on the applied gate voltage V_G at room temperature are shown in Figure 2a. The charge neutrality

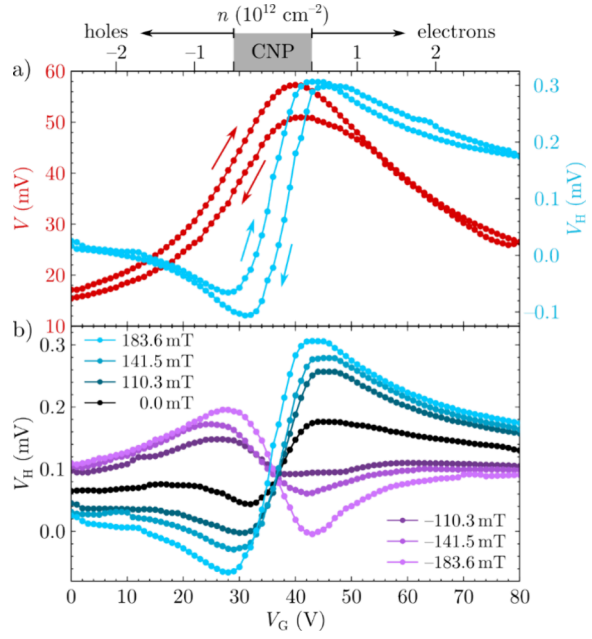

Figure 2. Representative response of the passivated graphene Hall probes to the application of the gate voltage at room temperature. (a) Both the longitudinal voltage V and the Hall voltage V_H exhibit hysteresis between the forward and backward sweep of the gate voltage V_G. (b) Variation of magnetic field and polarity causes a proportional response in the Hall voltage V_H (hysteresis is omitted for clarity and only forward sweeps are shown).

point at $V_{CNP} \approx 40$ V indicates the initial p-doping of the graphene layer which can be caused by residues from the lithographic processes[22] and by water molecules adsorbed either on top of the graphene layer or trapped between the SiO_2 and graphene.[23,24] Additionally, the presence of water molecules introduces a hysteresis between the forward and backward sweeps of the gate voltage V_G into all measurements.[23] In the following text, only the data obtained from the forward sweep of the gate voltage is presented, and the hysteretic behavior is omitted for clarity.

Figure 2b depicts the response of the graphene Hall probes to magnetic fields of varying magnitude and opposite polarities. A larger magnetic field generates a larger response, but there is also a nonzero response for a zero magnetic field. This so-called offset Hall voltage can generally arise from heterogeneity in the Hall element (local doping from adsorbents, electron–hole puddles, and trapped charges between material interfaces[25,26]) and from the geometry of the Hall element (its dimensions, contact size and placement, and potential misalignment between the Hall element and contacts[27]). The presence of this offset voltage explains the asymmetrical Hall voltage response where $V_H \approx 0.1$ mV corresponds to $V_G \approx V_{CNP}$ instead of the expected $V_H = 0$ mV. From the dependence of the Hall voltage on the applied magnetic field, we have been able to calculate the Hall coefficient $R_H = I^{-1} \cdot \partial V_H / \partial B$ as a function of the applied gate voltage V_G across the measured temperature range $T = (25-150)$ °C, Figure 3. The Hall coefficient R_H, being proportional to the slope of the linear fit of $V_H(B)$ (see the inset in Figure 3), is equal to the current-related sensitivity S_I which is sometimes used in the literature instead. The transfer curves shift to higher positive gate voltages with an increasing temperature (Supporting Information, Figures S7–S9), which is also reflected in the continual shift of the calculated dependence of the Hall coefficient.

In this work, the performance of Hall probes based on three graphene structures is compared: 10 μm wide graphene Hall bars with and without an SU-8 passivation layer, and graphene Hall bar constricted to 1 μm in the middle with the same passivation layer. Figure 4a plots the maximum achieved Hall coefficient in dependence on temperature for each of the three Hall probe types. From room temperature up to $T = 100$ °C, the passivated 10 μm Hall bar exhibits the highest Hall coefficient, although both passivated Hall bar types show higher response in the whole temperature range compared to the uncovered Hall bars exposed to air. Only the Hall coefficient of the passivated 10 μm Hall bar significantly decreases with temperature, whereas the passivated constricted Hall bar shows a slight increase, and the exposed 10 μm Hall bar remains almost stable across the measured temperature range.

Although each of the three Hall bar types performs differently with an increase in temperature, their resolution remains comparable independent of temperature, Figure 4b. Here, we calculate the resolution as the mean deviation of V_H data points from the linear fit of $V_H(B)$.[28] The resolution then reflects the stability of the linear operation of the graphene Hall probes with an increasing temperature.

3.2. Discussion. The majority of graphene Hall probe research focuses on low- to room-temperature measurements. Most of the Hall coefficient values reported in the literature for Hall probes based on CVD graphene tuned by electrostatic gating at room temperature fall into the range (1000–1550) Ω/T, Table 1. Although some studies have shown lower values, this can be attributed in most cases to the small dimensions of graphene elements ($w < 1\ \mu$m) due to an increased edge disorder and electronic noise.[14] The highest Hall coefficient obtained at 25 °C from the fabricated graphene Hall probes in this work was 1344 Ω/T, which is comparable to the published values. Additionally, the devices with the SU-8 passivation layer fabricated in this study consistently exhibit higher Hall coefficient than those exposed to air, which is in

https://doi.org/10.1021/acsaelm.5c00351
ACS Appl. Electron. Mater. 2025, 7, 5889–5897

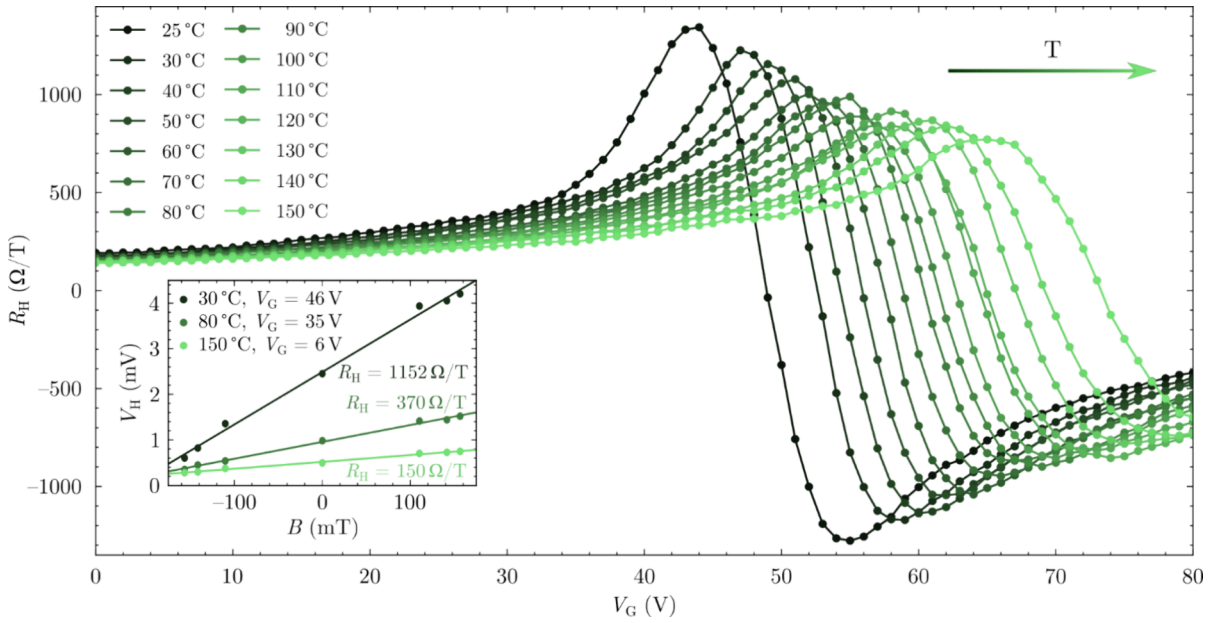

Figure 3. Hall coefficient R_H response of the passivated graphene Hall probe to the applied gate voltage V_G in the temperature range T = (25−150) °C and magnetic field B from −183.6 to 183.6 mT. The linear dependence of the measured Hall voltage on the applied magnetic field is depicted in the inset for various temperatures and gate voltages. The gate voltages were selected to represent varying doping levels in graphene, in particular, the low charge carrier density regime near CNP and higher carrier density regimes farther away from the CNP.

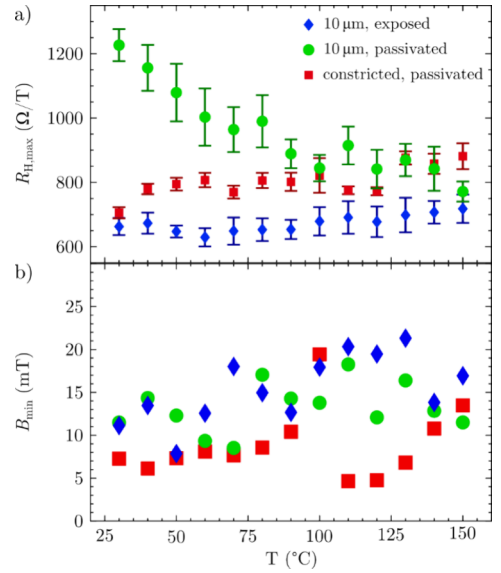

Figure 4. Calculated maximum Hall coefficients (a) and resolution (b) across the temperature range T = (30−150) °C for three types of graphene Hall elements: 10 μm graphene Hall bar exposed to air (blue), 10 μm graphene Hall bar covered by SU-8 (green), and constricted Hall bar covered by SU-8 (red).

agreement with reports for graphene Hall probes covered with dielectric[17,27] and polymer thin films.[16,28−30]

At 150 °C, the maximal values of the Hall coefficient achieved for our devices ranged between (720−880) Ω/T (Figure 4a), which are the highest values so far reported for graphene Hall probes at this temperature (Table 2), although other studies have also exposed graphene Hall probes to higher temperatures (even up to 500 °C[17]). The main reason for achieving such high values in this work is the combination of the passivation layer and the use of the solid-state bottom gate for tuning of the electronic properties of graphene, as can be seen in Figures 3 and 4a. Even though the benefits of passivation diminish with temperature, the option of tuning graphene properties by gating is essential for maximizing sensitivity regardless of the temperature. If we consider only values measured at V_G = 0 V in Figure 3, then the Hall coefficient reaches only 193 Ω/T at 25 °C and 142 Ω/T at 150 °C. In this case, the decrease with temperature is primarily caused by the shift of the transfer curves to positive gate voltages. Without this shift, the Hall coefficient at V_G = 0 V would remain the same across the measured temperature range, similar to the already observed results.[6,17,18] However, gate sweeping enables the measurement of extremes, which are 1344 and −1277 Ω/T at 25 °C in Figure 3, decreasing to 771 and −646 Ω/T at 150 °C. The maximum and minimum values differ probably a result of the hysteresis effects present in the device.

Each of the three Hall bar types demonstrates different behavior with increasing temperature. The 10 μm wide graphene Hall bar exposed to air exhibits almost a constant Hall coefficient, whereas the Hall coefficient continuously decreases for the passivated 10 μm Hall bar and even slightly increases for the constricted Hall bar with the passivation layer. It is assumed that adsorbents and air humidity do not affect graphene passivated by SU-8. Consequently, the 10 μm passivated Hall bar is affected only by temperature, and the decrease in Hall coefficient can be attributed to the charge carrier mobility decreasing with temperature as a consequence of a charge carrier-phonon interaction. By constricting the main channel of the Hall bar to 1 μm, the influence of edges is amplified. As a result, the Hall coefficient of the constricted and passivated Hall bar at 30 °C is significantly lower (705 Ω/T) than that one for the 10 μm passivated Hall bar (1227 Ω/T). Hence, we hypothesize that the higher presence of structural defects (vacancies and grain boundaries) at the edges and inside the lithographically narrowed graphene channel can be a primary factor determining the mobility of charge carriers

https://doi.org/10.1021/acsaelm.5c00351
ACS Appl. Electron. Mater. 2025, 7, 5889−5897

Table 1. Comparison of the Maximal Hall Coefficients R_H Achieved in This Work and Reported in the Literature for CVD-Grown Graphene Hall Probes Based on Field-Effect Transistors and Working at Room Temperature[a]

ref.	R_H (Ω/T)	I (μA)	w (μm)	μ (cm^2 V^{-1} s^{-1})	passivation
31	5030	1	6	12,000	240 nm PMMA
32	2745	100	15	7800	N/A
15	1550	100	2	5000	N/A
26	1270	N/A	7	5300, 4830	N/A
33	1230	100−1000	8	3423 ± 1045	N/A
29	1000	100	15	5100	1 μm SU-8
27	1076	500	25	2000	30 nm Al_2O_3
10	1200	3	5	N/A	N/A
14	140	12	0.085	840	N/A
34	345	15	0.5	133	exfoliated hBN
35	464	1	30	2168, 2598	N/A
this work	1230	10	10	2216, 3496	500 nm SU-8

[a]Other parameters include the driving current I, the width of the graphene element w, reported mobility μ (separately hole and electron mobilities μ_h, μ_e where applicable), and passivation of the sensor.

Table 2. Comparison of the Maximal Hall Coefficients R_H Achieved in This Work and Reported in the Literature for Graphene Hall Probes at 150 °C[a]

ref.	graphene	R_H (Ω/T)	I (μA)	w (μm)	μ (cm^2 V^{-1} s^{-1}) at RT	μ (cm^{2}V^{-1} s^{-1}) at 150 °C
17	epitaxial	80	1000	100	3344	2750
36	epitaxial	78	1000	100	1650	1500
37	epitaxial	74	1000	100	1900	1700
6	epitaxial	100	N/A	90	695	N/A
19	epitaxial	300	400	30−140	2300	N/A
18	CVD	40	300	N/A	N/A	N/A
this work	CVD	700−900	10	10	2216, 3496	1193, 2080

[a]The graphene layers used in the studies were either grown epitaxially by CVD directly on a SiC substrate ("epitaxial") or grown by CVD on a metal foil and then transferred onto the target substrate ("CVD"). Other parameters include the driving current I, the width of the graphene element w, and mobility μ at room temperature and at 150 °C (separately hole and electron mobilities μ_h, μ_e where applicable).

and prevailing over the effect of temperature. Therefore, the Hall coefficient is approximately constant, and a moderate growth with temperature could be attributed to the elimination of defects by a higher diffusion of atoms and interstitials. For the 10 μm graphene Hall bar exposed to air, desorption of water molecules from graphene with increasing temperature must be considered. In this case, the detrimental effect of decreasing mobility with temperature might be compensated by the removal of adsorbed water molecules, and the Hall coefficient roughly remains constant in the measured temperature range.

The hypothesis of a higher concentration of defects in the constricted graphene Hall bar is further supported by a Raman spectroscopy mapping performed before the application of the passivation layer, Figure 5. Although both Hall bar types show higher intensity of the D peak compared to the transferred graphene layer before patterning, the constricted Hall bar is characterized by higher values of the D peak intensity overall, i.e., not only in the constricted part of the graphene channel. This can be caused by differences in the lithographic processing that can subsequently result in a varying adhesion of graphene on the substrate or the presence of the resist on graphene. Multiple lithographic steps also lead to successive degradation of the graphene layer quality (Supporting Information, Figure S2).

From the calculated values of the Hall coefficient R_H, the mobility of charge carriers in dependence on the gate voltage V_G and temperature T can be obtained according to the formula $\mu = R_H/\rho_s(B = 0)$, where R_H is the Hall coefficient and

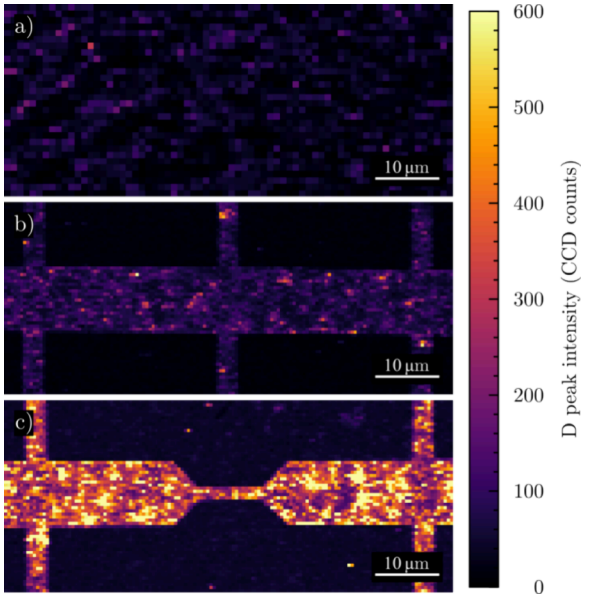

Figure 5. Mapping of the intensity of the D peak in the Raman spectra of (a) graphene layer after its transfer onto the substrate, (b) patterned 10 μm graphene Hall bar, and (c) patterned constricted graphene Hall bar.

ρ_s is the sheet resistivity without an applied magnetic field B. Figure 6a depicts mobility as a function of gate voltage for T = 30 °C where the mobility of holes steadily increases until a maximal value of 2945 cm^2 V^{-1} s^{-1} at V_G = 46 V, which is

https://doi.org/10.1021/acsaelm.5c00351
ACS Appl. Electron. Mater. 2025, 7, 5889−5897

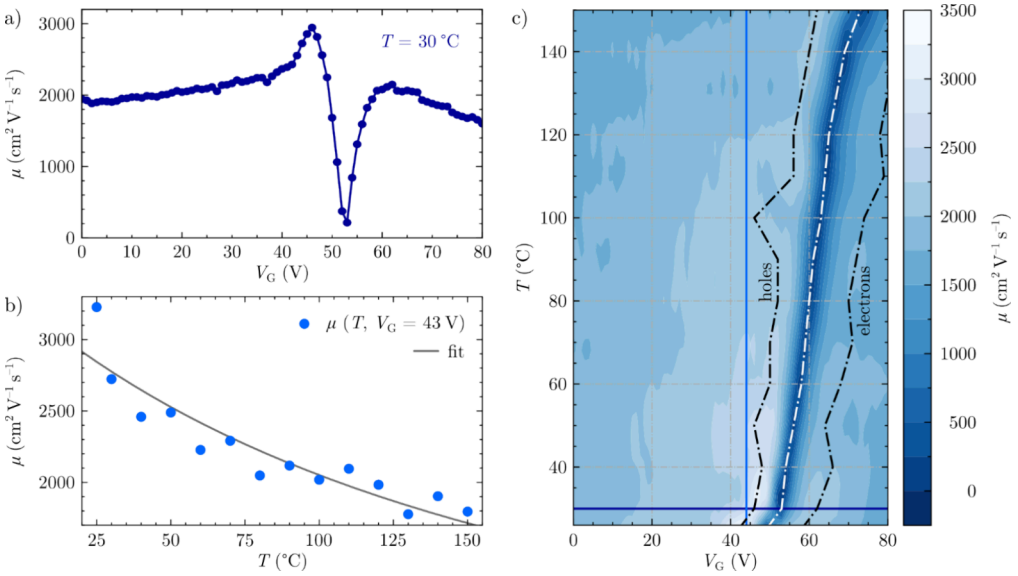

Figure 6. Mobility of charge carriers in graphene as a function of the gate voltage V_G and temperature T. (a) Dependence of the mobility on the gate voltage at a constant temperature of 30 °C and (b) temperature evolution of mobility for constant gate voltage V_G = 43 V with a fit of the measured data based on the scattering model described in the text. (c) Calculated mobility as a function of both gate voltage and temperature. The dot-dashed lines connect the experimental values of the maximum hole mobility, mobility minimum, and maximum electron mobility at each measured temperature.

followed by a sharp decrease to the minimum at V_G = 53 V. Similarly, electron mobility peaks at 2148 cm^2 V^{-1} s^{-1} at V_G = 62 V and slowly decreases with increasing charge carrier density.

At any given temperature, mobility reaches its minimum around the charge neutrality point and the sharp decrease between the minimal and maximal values with an increasing carrier density can be attributed to a nonlinear dependence of resistivity on the charge carrier concentration resulting from short and long-range scattering,[38] Figure 6a. With an increasing temperature, electron−phonon interaction becomes the main contributor to inelastic scattering in graphene[39] which causes the decrease of mobility depicted in Figure 6b. The temperature evolution of the mobility should follow the predicted dependence in eq 1 for a constant charge carrier density. Although this condition is not strictly fulfilled for the mobility extracted at a constant gate voltage V_G—since the carrier density is affected by the temperature-induced shift of the transfer curves toward more positive gate voltages — the fit still provides a reasonably good agreement with the experimental data in Figure 6b. Figure 6c shows the mobility as a function of the gate voltage calculated in a measured temperature range of (25−150) °C from the curves in Figure 3. The shift of the transfer curves to positive gate voltages with increasing temperatures is also reflected in the shift of the mobility extremes for charge carriers as illustrated by the dot-dashed lines.

At low temperatures, the mobility of graphene is primarily affected by scattering on impurities, structural defects, and grain boundaries, all of which are characterized by temperature-independent relaxation times τ. Additionally, scattering by acoustic phonons intrinsic to graphene is relevant in this low-temperature range, which exhibits an inverse temperature dependence. As the temperature increases, charge carrier scattering induced by the substrate becomes the prevailing factor. In our case, surface optical phonons originating from the SiO_2 substrate and the SU-8 resist play the dominant role in the high-temperature regime.[40] The temperature dependence of the charge carrier relaxation time from scattering on SiO_2 surface phonons can be modeled using the inverse Bose−Einstein distribution $\tau_{SiO_2} \propto e^{\omega/k_BT} - 1$, where ω corresponds to a surface optical phonon mode with an energy of 59 meV. Due to the amorphous nature of the SU-8 layer, the relaxation time associated with its surface phonons τ_{SU-8} is assumed to follow a $1/T$ dependence. The total mobility μ_{tot} is then given by

$$\frac{1}{\mu_{tot}} = \frac{1}{\mu_{SiO_2}} + \frac{1}{\mu_{SU-8}} = \frac{1}{A(e^{\omega/k_BT} - 1)} + \frac{1}{B/T} \quad (1)$$

where A and B are fitting parameters.[41] It is worth noting that the term μ_{SU-8} may also implicitly include contributions from acoustic phonons in graphene, which exhibit the same inverse temperature dependence and are, therefore, indistinguishable within this model. However, their contribution to the total mobility is expected to be negligible in the measured temperature range. The fit of this model is shown in Figure 6b for calculated mobility values at a constant gate voltage V_G = 43 V, where the fitting parameters are A = 1257 cm^2 V^{-1} s^{-1} and B = 1.243 × 10^6 cm^2 V^{-1} s^{-1} K.

In the case of the exposed sample, the mobility contribution from the SU-8 layer is no longer present. Instead, a new scattering channel related to the adsorbed water molecules emerges, represented by a mobility term μ_{H_2O}. The water molecules represent charged impurities, whose number decreases with the temperature. The total mobility can be then expressed as follows:

$$\frac{1}{\mu_{tot}} = \frac{1}{\mu_{SiO_2}} + \frac{1}{\mu_{H_2O}} \quad (2)$$

where

https://doi.org/10.1021/acsaelm.5c00351
ACS Appl. Electron. Mater. 2025, 7, 5889−5897

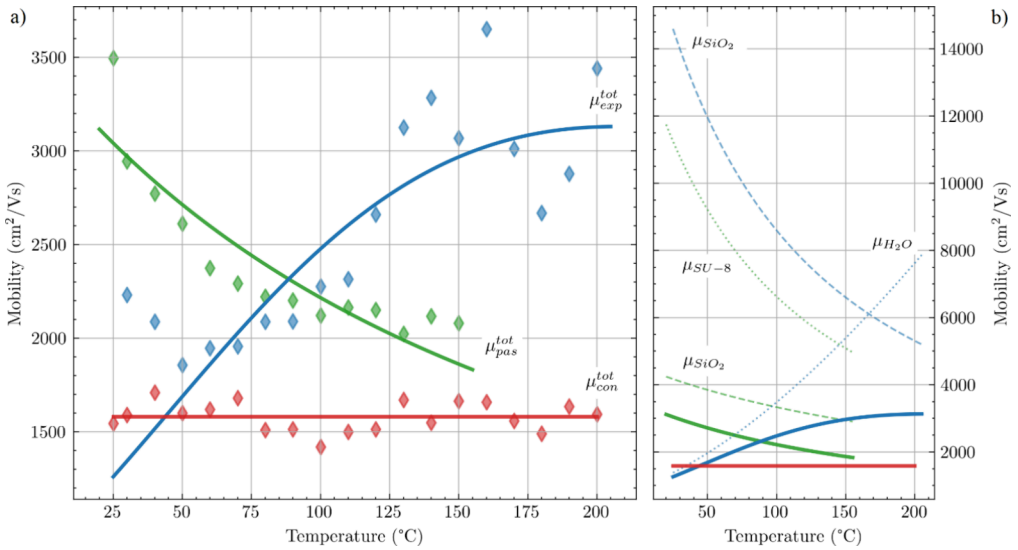

Figure 7. Summary of all the scattering mechanisms observed in performed experiments and their impact on charge carrier mobility: for passivated sample (green), exposed sample (blue), and constricted sample (red). (a) Experimentally measured mobility (points) for constant gate voltage V_G = 43 V is interpolated by the corresponding model (solid curves). (b) Contribution of partial scattering mechanism to the overall model: SiO_2 phonons (green and blue dashed lines), SU-8 phonons (green dotted line), H_2O-induced scattering (blue dotted line). All the fitted parameters are summarized in the Supporting Information.

$$\mu_{H_2O} = \frac{\mu_0}{\theta(T)} \tag{3}$$

where μ_0 is the minimal mobility corresponding to the complete coverage of the graphene surface by water molecules. The surface coverage $\theta(T)$ is possible to describe using the Langmuir adsorption isotherm[42]:

$$\theta(T) = \frac{b(T)P}{1 + b(T)P},\ b(T) = b_0 e^{-E_{ads}/k_B T} \tag{4}$$

where P = 924 Pa is the partial pressure of water vapor corresponding to the relative humidity, and b is the adsorption equilibrium constant given by Boltzmann distribution, b_0 is the preexponential factor and E_{ads} = −122.44 meV is the adsorption energy of water molecule.[43] Due to negative adsorption energy, the coverage decreases with temperature, which leads to an increase of the mobility limited by water. Including the water contribution, the total mobility of the exposed sample can be expressed as

$$\frac{1}{\mu_{tot}} = \frac{1}{A(e^{\omega/k_B T} - 1)} + \frac{Pb_0 \cdot e^{-E_{ads}/k_B T}}{\mu_0 \cdot (1 + Pb_0 \cdot e^{-E_{ads}/k_B T})} \tag{5}$$

where A, b_0 and μ_0 are the fitting parameters. The fit of this model is shown in Figure 7 (blue) for calculated mobility values at a constant gate voltage V_G = 43 V, where the fitting parameters are A = 3043 cm^2 V^{-1} s^{-1}, b_0 = 1.938 × 10^{-5} Pa^{-1} and μ_0 = 1251 cm^2 V^{-1} s^{-1}.

For the constrained system, the graphene layer is already significantly perturbed by defects. As a result, the graphene lattice defects become the dominant scattering mechanism. Since the impact of defects on charge carrier mobility is largely temperature-independent,[44] the total mobility of the constricted sample can be expressed as

$$\frac{1}{\mu_{tot}} = \frac{1}{\mu_{def}} \tag{6}$$

where μ_{def} = 1580 cm^2 V^{-1} s^{-1} is the defect contribution to the mobility given by fitting the appropriate experimentally observed mobility.

The presented models can completely describe the results of measured mobility as seen in Figure 7. The decrease of mobility of the passivated sample with the temperature can be explained by the minority role SU-8 (green dotted line) and the majority role of SiO_2 phonons (green dashed line). The exposed sample exhibits the increase of mobility as a function of temperature since the main limiting scattering mechanism is water adsorbed on the surface at room temperature that gradually evaporates as the sample is heated up (blue dotted line). From this point of view, the exposed sample, free from the SU-8 photoresist-related scattering mechanisms and free from water at high temperatures, could be a great Hall probe. However, the measured Hall coefficients (Figure 4a) are lower and constant due to decreased sheet resistance during water evaporation. Finally, the mobility of the constricted channel is entirely governed by a large amount of lattice defects independent of temperature in the studied temperature range.

A critical question for graphene sensors is their long-term stability in ambient conditions. Previous studies have shown that graphene Hall probes without any passivation layer slowly degrade over time. Iyer et al. measured the performance of their sensors after 42 days on air and saw a decrease of the Hall coefficient from 1.13 to 0.92 kΩ/T.[26] In contrast, Tyagi et al. observed a significant reduction in hysteresis and improved stability over 10 weeks for a sensor passivated with a thin layer of PMMA, compared to a sensor with the graphene layer exposed to air.[31] Other studies also demonstrated that graphene encapsulated with CVD-grown hBN[45] or parylene C[46] can exhibit excellent stability over several months. It should be noted that in commercial electronics, the chips are typically sealed with thick oxide layers to prevent degradation of the semiconducting and metallic parts.

https://doi.org/10.1021/acsaelm.5c00351
ACS Appl. Electron. Mater. 2025, 7, 5889−5897

4. CONCLUSIONS

In this work, we have fabricated and tested Hall probes based on CVD-grown graphene employing a field effect transistor architecture. We have simultaneously measured the Hall effect response and transfer characteristics of these sensors from room temperature up to 150 °C. Our results show that tuning graphene properties by the field effect is essential for maximizing the sensitivity of the device and that adding a passivation layer improves the sensor response even at higher temperatures. Furthermore, the sensitivities in a range of (720−880) Ω/T achieved in this work at 150 °C are, so far, the highest reported values for graphene Hall probes at elevated temperatures. Based on the obtained results, we have calculated the temperature evolution of the charge carrier mobility in dependence on the applied gate voltage and developed models based on various contributions to mobility, which completely describe the results for the three studied sensor designs. Although the device performance slowly deteriorates with increasing temperature, graphene Hall probes are an excellent choice for high-temperature applications due to their high sensitivity across a large temperature range.

■ ASSOCIATED CONTENT

Data Availability Statement

The data that support the findings of this study are at: 10.5281/zenodo.15601462.

Supporting Information

The Supporting Information is available free of charge at https://pubs.acs.org/doi/10.1021/acsaelm.5c00351.

Additional experimental details, methods, measurements, and parameters for fitting of experimental data to the proposed models (PDF)

■ AUTHOR INFORMATION

Corresponding Author

Miroslav Bartošík − *Central European Institute of Technology−Brno University of Technology (CEITEC BUT), 612 00 Brno, Czech Republic; Institute of Physical Engineering, Brno University of Technology, 616 69 Brno, Czech; Department of Physics and Materials Engineering Faculty of Technology, Tomas Bata University in Zlín, 760 01 Zlín, Czech Republic;* orcid.org/0000-0003-4706-9112; Email: bartosik@fme.vutbr.cz

Authors

Linda Supalová − *Central European Institute of Technology−Brno University of Technology (CEITEC BUT), 612 00 Brno, Czech Republic; Institute of Physical Engineering, Brno University of Technology, 616 69 Brno, Czech*

Vojtěch Švarc − *Central European Institute of Technology−Brno University of Technology (CEITEC BUT), 612 00 Brno, Czech Republic*

Jindřich Mach − *Central European Institute of Technology−Brno University of Technology (CEITEC BUT), 612 00 Brno, Czech Republic; Institute of Physical Engineering, Brno University of Technology, 616 69 Brno, Czech*

Jakub Piastek − *Central European Institute of Technology−Brno University of Technology (CEITEC BUT), 612 00 Brno, Czech Republic; Institute of Physical Engineering, Brno University of Technology, 616 69 Brno, Czech*

Ondřej Špaček − *Central European Institute of Technology−Brno University of Technology (CEITEC BUT), 612 00 Brno, Czech Republic; Institute of Physical Engineering, Brno University of Technology, 616 69 Brno, Czech*

Martin Konečný − *Central European Institute of Technology−Brno University of Technology (CEITEC BUT), 612 00 Brno, Czech Republic; Institute of Physical Engineering, Brno University of Technology, 616 69 Brno, Czech*

Tomáš Šikola − *Central European Institute of Technology−Brno University of Technology (CEITEC BUT), 612 00 Brno, Czech Republic; Institute of Physical Engineering, Brno University of Technology, 616 69 Brno, Czech*

Complete contact information is available at: https://pubs.acs.org/10.1021/acsaelm.5c00351

Notes

The authors declare no competing financial interest.

■ ACKNOWLEDGMENTS

We acknowledge the support by the Grant Agency of the Czech Republic (Grant No. 25-16894S), OP JAK (Project No. CZ.02.01.01/00/22_008/0004594 TERAFIT), MEYS CR (Project No. LQ1601−CEITEC 2020), and CzechNanoLab Research Infrastructure supported by MEYS CR (LM2023051).

■ REFERENCES

(1) Kejik, P.; Boero, G.; Demierre, M.; Popovic, R. S. An Integrated Micro-Hall Probe for Scanning Magnetic Microscopy. *Sensors and Actuators A: Physical* **2006**, *129* (1−2), 212−215.

(2) Goel, N.; Babuta, A.; Kumar, A.; Ganguli, S. Hall Effect Instruments, Evolution, Implications, and Future Prospects. *Rev. Sci. Instrum.* **2020**, *91* (7), No. 071502.

(3) Zaim, S.; Martin, J. P.; Nahid-Mobarakeh, B.; Meibody-Tabar, F. High Performance Low Cost Control of a Permanent Magnet Wheel Motor Using a Hall Effect Position Sensor. In *2011 IEEE Vehicle Power and Propulsion Conference*; IEEE: Chicago, IL, USA, 2011; 1−6.

(4) Crescentini, M.; Syeda, S. F.; Gibiino, G. P. Hall-Effect Current Sensors: Principles of Operation and Implementation Techniques. *IEEE Sensors J.* **2022**, *22* (11), 10137−10151.

(5) Jogschies, L.; Klaas, D.; Kruppe, R.; Rittinger, J.; Taptimthong, P.; Wienecke, A.; Rissing, L.; Wurz, M. Recent Developments of Magnetoresistive Sensors for Industrial Applications. *Sensors* **2015**, *15* (11), 28665−28689.

(6) Reddig, W.; Przychodnia, M.; Ciuk, T.; El-Ahmar, S. High-Temperature Stability of Sensor Platforms Designed to Detect Magnetic Fields in a Harmful Radiation Environment. *IEEE Sens. Lett.* **2023**, *7* (8), 1−4.

(7) Vervaeke, K.; Simoen, E.; Borghs, G.; Moshchalkov, V. V. Size Dependence of Microscopic Hall Sensor Detection Limits. *Rev. Sci. Instrum.* **2009**, *80* (7), No. 074701.

(8) Kazakova, O.; Gallop, J. C.; Cox, D. C.; Brown, E.; Cuenat, A.; Suzuki, K. Optimization of 2DEG InAs/GaSb Hall Sensors for Single Particle Detection. *IEEE Trans. Magn.* **2008**, *44* (11), 4480−4483.

(9) Sandhu, A.; Sanbonsugi, H.; Shibasaki, I.; Abe, M.; Handa, H. High Sensitivity InSb Ultra-Thin Film Micro-Hall Sensors for Bioscreening Applications. *Jpn. J. Appl. Phys.* **2004**, *43* (7A), L868.

(10) Tang, C.-C.; Li, M.-Y.; Li, L. J.; Chi, C. C.; Chen, J. C. Characteristics of a Sensitive Micro-Hall Probe Fabricated on Chemical Vapor Deposited Graphene over the Temperature Range

from Liquid-Helium to Room Temperature. *Appl. Phys. Lett.* **2011**, *99* (11), 112107.
(11) Huang, L.; Zhang, Z.; Chen, B.; Ma, X.; Zhong, H.; Peng, L.-M. Ultra-Sensitive Graphene Hall Elements. *Appl. Phys. Lett.* **2014**, *104* (18), 183106.
(12) Schaefer, B. T.; Wang, L.; Jarjour, A.; Watanabe, K.; Taniguchi, T.; McEuen, P. L.; Nowack, K. C. Magnetic Field Detection Limits for Ultraclean Graphene Hall Sensors. *Nat. Commun.* **2020**, *11* (1), 4163.
(13) Dauber, J.; Sagade, A. A.; Oellers, M.; Watanabe, K.; Taniguchi, T.; Neumaier, D.; Stampfer, C. Ultra-Sensitive Hall Sensors Based on Graphene Encapsulated in Hexagonal Boron Nitride. *Appl. Phys. Lett.* **2015**, *106* (19), 193501.
(14) Collomb, D.; Li, P.; Bending, S. J. Nanoscale Graphene Hall Sensors for High-Resolution Ambient Magnetic Imaging. *Sci. Rep* **2019**, *9* (1), 14424.
(15) Xu, H.; Zhang, Z.; Shi, R.; Liu, H.; Wang, Z.; Wang, S.; Peng, L.-M. Batch-Fabricated High-Performance Graphene Hall Elements. *Sci. Rep* **2013**, *3* (1), 1207.
(16) Dai, T.; Chen, C.; Huang, L.; Jiang, J.; Peng, L.-M.; Zhang, Z. Ultrasensitive Magnetic Sensors Enabled by Heterogeneous Integration of Graphene Hall Elements and Silicon Processing Circuits. *ACS Nano* **2020**, *14* (12), 17606−17614.
(17) Ciuk, T.; Stanczyk, B.; Przyborowska, K.; Czolak, D.; Dobrowolski, A.; Jagiello, J.; Kaszub, W.; Kozubal, M.; Kozlowski, R.; Kaminski, P. High-Temperature Hall Effect Sensor Based on Epitaxial Graphene on High-Purity Semiinsulating 4H-SiC. *IEEE Trans. Electron Devices* **2019**, *66* (7), 3134−3138.
(18) Peters, A.; Turvey, S.; Horsfall, A. B. High Temperature Graphene Sensors for Harsh Environment Current Sensing. In *2019 IEEE Sensors*; IEEE: Montreal, QC, Canada, 2019; 1−4.
(19) He, H.; Shetty, N.; Bauch, T.; Kubatkin, S.; Kaufmann, T.; Cornils, M.; Yakimova, R.; Lara-Avila, S. The Performance Limits of Epigraphene Hall Sensors Doped across the Dirac Point. *Appl. Phys. Lett.* **2020**, *116* (22), 223504.
(20) Li, X.; Zhu, Y.; Cai, W.; Borysiak, M.; Han, B.; Chen, D.; Piner, R. D.; Colombo, L.; Ruoff, R. S. Transfer of Large-Area Graphene Films for High-Performance Transparent Conductive Electrodes. *Nano Lett.* **2009**, *9* (12), 4359−4363.
(21) ASTM International. *Test Methods for Measuring Resistivity and Hall Coefficient and Determining Hall Mobility in Single-Crystal Semiconductors*; ASTM International, 2023.
(22) Pirkle, A.; Chan, J.; Venugopal, A.; Hinojos, D.; Magnuson, C. W.; McDonnell, S.; Colombo, L.; Vogel, E. M.; Ruoff, R. S.; Wallace, R. M. The Effect of Chemical Residues on the Physical and Electrical Properties of Chemical Vapor Deposited Graphene Transferred to SiO2. *Appl. Phys. Lett.* **2011**, *99* (12), 122108.
(23) Bartošík, M.; Mach, J.; Piastek, J.; Nezval, D.; Konečný, M.; Švarc, V.; Ensslin, K.; Šikola, T. Mechanism and Suppression of Physisorbed-Water-Caused Hysteresis in Graphene FET Sensors. *ACS Sens.* **2020**, *5* (9), 2940−2949.
(24) Švarc, V.; Bartošík, M.; Konečný, M.; Piastek, J.; Nezval, D.; Mach, J.; Šikola, T. Side Charge Propagation in Simultaneous KPFM and Transport Measurement of Humidity Exposed Graphene FET Sensor. *Carbon* **2023**, *215*, No. 118471.
(25) Das, S.; Sebastian, A.; Pop, E.; McClellan, C. J.; Franklin, A. D.; Grasser, T.; Knobloch, T.; Illarionov, Y.; Penumatcha, A. V.; Appenzeller, J.; Chen, Z.; Zhu, W.; Asselberghs, I.; Li, L.-J.; Avci, U. E.; Bhat, N.; Anthopoulos, T. D.; Singh, R. Transistors Based on Two-Dimensional Materials for Future Integrated Circuits. *Nat. Electron* **2021**, *4* (11), 786−799.
(26) Iyer, V.; Johnson, A. T. C.; Aflatouni, F.; Issadore, D. A. Mitigation of Device Heterogeneity in Graphene Hall Sensor Arrays Using Per-Element Backgate Tuning. *ACS Appl. Mater. Interfaces* **2024**, *16* (30), 39761−39770.
(27) Polley, A.; Ravichandran, A. V.; Kumar, V. S.; Venugopal, A.; Cheng, L.; Lucero, A. T.; Kim, J.; Colombo, L.; Doering, R. R. Ambipolar Gate Modulation Technique for the Reduction of Offset and Flicker Noise in Graphene Hall-Effect Sensors. *IEEE Sensors J.* **2021**, *21* (22), 25675−25686.
(28) Gerken, M.; Solignac, A.; Momeni Pakdehi, D.; Manzin, A.; Weimann, T.; Pierz, K.; Sievers, S.; Schumacher, H. W. Traceably Calibrated Scanning Hall Probe Microscopy at Room Temperature. *J. Sens. Sens. Syst.* **2020**, *9* (2), 391−399.
(29) Xu, H.; Huang, L.; Zhang, Z.; Chen, B.; Zhong, H.; Peng, L.-M. Flicker Noise and Magnetic Resolution of Graphene Hall Sensors at Low Frequency. *Appl. Phys. Lett.* **2013**, *103* (11), 112405.
(30) Wang, Z.; Banszerus, L.; Otto, M.; Watanabe, K.; Taniguchi, T.; Stampfer, C.; Neumaier, D. Encapsulated Graphene-Based Hall Sensors on Foil with Increased Sensitivity: Encapsulated Graphene-Based Hall Sensors. *Phys. Status Solidi B* **2016**, *253* (12), 2316−2320.
(31) Tyagi, A.; Martini, L.; Gebeyehu, Z. M.; Mišeikis, V.; Coletti, C. Highly Sensitive Hall Sensors Based on Chemical Vapor Deposition Graphene. *ACS Appl. Nano Mater.* **2024**, *7* (16), 18329−18336.
(32) Chen, B.; Huang, L.; Ma, X.; Dong, L.; Zhang, Z.; Peng, L.-M. Exploration of Sensitivity Limit for Graphene Magnetic Sensors. *Carbon* **2015**, *94*, 585−589.
(33) Sun, H.; Huang, T.; Alam, M. M.; Li, J.; Jang, D. W.; Wang, T.; Chen, H.; Ho, Y.-P.; Gao, Z. Minimizing Contact Resistance and Flicker Noise in Micro Graphene Hall Sensors Using Persistent Carbene Modified Gold Electrodes. *ACS Appl. Mater. Interfaces* **2024**, *16* (24), 31473−31479.
(34) Karpiak, B.; Dankert, A.; Dash, S. P. Gate-Tunable Hall Sensors on Large Area CVD Graphene Protected by h-BN with 1D Edge Contacts. *J. Appl. Phys.* **2017**, *122* (5), No. 054506.
(35) Song, G.; Ranjbar, M.; Kiehl, R. A. Operation of Graphene Magnetic Field Sensors near the Charge Neutrality Point. *Commun. Phys.* **2019**, *2* (1), 65.
(36) Ciuk, T.; Kozłowski, R.; Romanowska, A.; Zagojski, A.; Piętak-Jurczak, K.; Stańczyk, B.; Przyborowska, K.; Czołak, D.; Kamiński, P. Defect-Engineered Graphene-on-Silicon-Carbide Platform for Magnetic Field Sensing at Greatly Elevated Temperatures. *Carbon Trends* **2023**, *13*, No. 100303.
(37) Ciuk, T.; Nouvellon, C.; Monteverde, F.; Stańczyk, B.; Przyborowska, K.; Czołak, D.; El-Ahmar, S. High-Temperature Thermal Stability of a Graphene Hall Effect Sensor on Defect-Engineered 4H-SiC(0001). *IEEE Electron Device Lett.* **2024**, *45* (10), 1957−1960.
(38) Hong, X.; Zou, K.; Zhu, J. Quantum Scattering Time and Its Implications on Scattering Sources in Graphene. *Phys. Rev. B* **2009**, *80* (24), No. 241415.
(39) Li, Q.; Das Sarma, S. Finite Temperature Inelastic Mean Free Path and Quasiparticle Lifetime in Graphene. *Phys. Rev. B* **2013**, *87* (8), No. 085406.
(40) Fratini, S.; Guinea, F. Substrate-Limited Electron Dynamics in Graphene. *Phys. Rev. B* **2008**, *77* (19), No. 195415.
(41) Zhu, W.; Perebeinos, V.; Freitag, M.; Avouris, P. Carrier Scattering, Mobilities, and Electrostatic Potential in Monolayer, Bilayer, and Trilayer Graphene. *Phys. Rev. B* **2009**, *80* (23), No. 235402.
(42) Zangi, R. Breakdown of Langmuir Adsorption Isotherm in Small Closed Systems. *Langmuir* **2024**, *40*, 3900−3910.
(43) Nezval, D.; Bartošík, M.; Mach, J.; Švarc, V.; Konečný, M.; Piastek, J.; Špaček, O.; Šikola, T. DFT Study of Water on Graphene: Synergistic Effect of Multilayer p-Doping. *J. Chem. Phys.* **2023**, *159* (21), 214710.
(44) Stauber, T.; Peres, N. M. R.; Guinea, F. Electronic Transport in Graphene: A Semiclassical Approach Including Midgap States. *Phys. Rev. B* **2007**, *76* (20), No. 205423.
(45) Dankert, A.; Karpiak, B.; Dash, S. P. Hall Sensors Batch-Fabricated on All-CVD h-BN/Graphene/h-BN Heterostructures. *Sci. Rep* **2017**, *7* (1), 15231.
(46) Alexandrou, K.; Petrone, N.; Hone, J.; Kymissis, I. Encapsulated Graphene Field-Effect Transistors for Air Stable Operation. *Appl. Phys. Lett.* **2015**, *106* (11), 113104.

https://doi.org/10.1021/acsaelm.5c00351
ACS Appl. Electron. Mater. 2025, 7, 5889−5897